



**kapteyn astronomical
institute**

UNIVERSITY OF GRONINGEN

BACHELOR'S THESIS

Measurements of the Mass and Radius of a Neutron Star: consequences for the Equation of State of dense nuclear matter

Author:
Tobias Vos

Supervisor:
Prof. dr. Mariano Méndez

July 3, 2015

ABSTRACT

The neutron star low-mass X-ray binary EXO 0748-676 started a transition from outburst to quiescence in 2008, after more than 24 years of continuous accretion. Here, I use the spectral fitting package XSPEC to analyse the X-ray spectra of four XMM-Newton observations, elapsing a period of over four years, that started in March 2009. I confirm that cooling NS models, modified by interstellar absorption, provide the best fits to the spectra. Both hydrogen and helium NS atmosphere models can account for the observed flux levels. I detect a gaussian line feature that accounts for $\sim 10\%$ of the total flux. From the spectral fits, I infer limits to the mass and radius of the neutron star. I find that the recent outburst cannot by itself account for the mass reached by the neutron star. By comparing the best-fit masses and radii to theoretical predictions, I find that none of the proposed equations of state for dense, cold nuclear matter can account for the mass and radius predicted by the helium atmosphere model. Therefore, I conclude that the NS atmosphere of EXO 0748-676 is mainly composed of hydrogen. Furthermore, I deduce that the internal composition of neutron stars is dominated by neutrons and protons, rather than hyperons, kaons or quark matter. Finally, I find that the line feature is most likely due to imperfections in the abundance and cross sections tables used to describe the interstellar medium. If it is a real emission line, it is presumably produced by highly ionised carbon in the NS atmosphere.

Contents

1	INTRODUCTION	2
2	OBSERVATIONS	4
2.1	XMM-Newton instruments	4
2.2	XMM-Newton observations	5
2.3	Data reduction	6
3	DATA ANALYSIS	7
3.1	Defining model spectra	7
3.2	Fitting model spectra	10
4	RESULTS	12
4.1	Best-fit models	12
4.2	Contour plots	13
4.3	Emission lines	15
5	DISCUSSION	16
5.1	Implications for the accretion rate and efficiency	16
5.2	Constraints on the dense matter equation of state	18
5.3	Origin of the emission line	20
6	CONCLUSIONS	22
	APPENDICES	23
A	Spectral fitting and XSPEC	23
B	Uncertainty calculations	24
	REFERENCES	25

1 INTRODUCTION

Low-mass X-ray binaries (LMXBs) are binary systems in which a low-mass star (usually a main sequence star with a mass lower than $1 M_{\odot}$), known as the ‘donor’, and a compact object (a black hole or a neutron star), known as the ‘accretor’, orbit around a common centre of mass. Due to the difference in their masses, and thus in the gravitational forces that they exert on each other, the compact object can attract (*accrete*) matter from the companion star. In LMXBs, this mass transfer happens mainly via Roche lobe overflow. The Roche lobe is the region around a star in a binary system in which orbiting material is gravitationally bound. If the surface of the donor is extended out beyond its Roche lobe (by the gravitational pull of the compact object), material which lies outside its Roche lobe can fall off into the accretor’s Roche lobe via the inner Lagrangian point, L_1 . The latter is the dynamically stable point between two large masses, where the gravitational and centrifugal (due to the orbital velocity of the material) forces balance.

As the material falls in, its high orbital angular momentum prevents direct radial accretion onto the compact object. Fortunately, viscosity and friction allow angular momentum to be transferred outwards as the matter moves inwards, creating a so-called *accretion disc*. As the matter spirals inwards, viscous stresses in the accretion disc convert some of its kinetic energy into heat (internal energy), heating it to temperatures of millions of degrees. As a result, the accretion disc is bright in the X-ray part of the electromagnetic spectrum, hence the name ‘low-mass X-ray binary’. At some point, when the material gets too close to the compact object, its gravitational pull disrupts the material’s stable ‘circular’ orbit, forcing it to plunge onto the compact object’s surface. This process converts part of the residual gravitational potential energy of the material into additional X-ray photons. See Figure 1 for a schematic representation of an accreting LMXB.¹

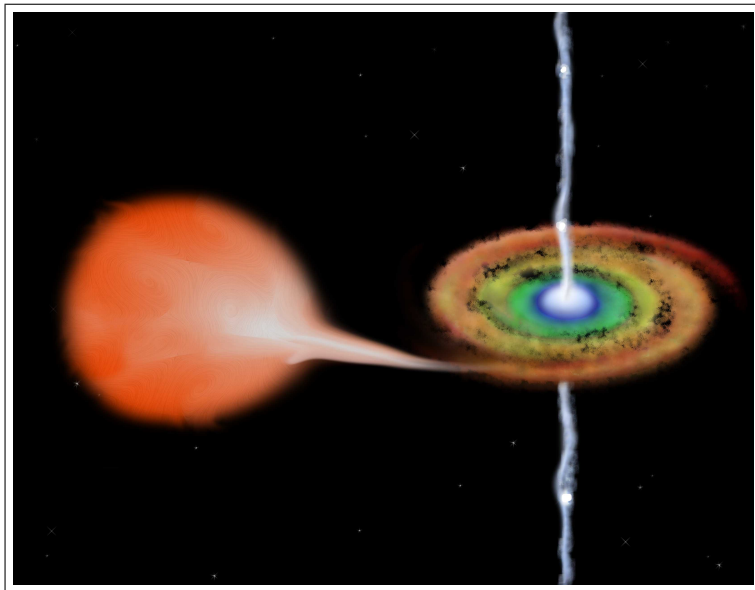


Figure 1: Artist’s conception of a low-mass X-ray binary. Gaseous matter from the companion star (left) accretes onto the compact object via an accretion disc (right). Intense electromagnetic forces in the disc can expel jets of high-energy matter.

¹Picture taken from the Chandra X-ray observatory website. Credit: CXC/M. Weiss

However, this accretion phase does not last forever. It all depends on the size of the companion star's Roche lobe, which in itself depends on the orbital separation and the masses of the two binary components. The onset of Roche lobe overflow usually requires that the companion star expands (due to stellar evolution) or that the orbit shrinks (due to losses of orbital angular momentum). This initiates an accretion phase which, in principle, could lead to the total disintegration of the donor, since a reduction of its mass causes its Roche lobe to shrink. Yet, there are several reasons why this does not happen in general. First, because a reduction of the mass of the donor star may cause the donor star to shrink as well, preventing such an outcome. Second, because angular momentum is also transferred. Under the assumption of mass and angular momentum conservation, mass transfer from a less massive donor to a more massive accretor causes the orbit to *expand*, leading to less dramatic shrinkage or even expansion of the donor's Roche lobe.

Because of these effects, there are two main classes of LMXBs: *persistent LMXBs* and *transient LMXBs*. Both classes emit most of their radiation in the X-ray part of the electromagnetic spectrum, but they differ in the way their X-ray flux changes with time. The flux of persistent LMXBs is near constant in time (since we started monitoring them, at least), while the flux of transient LMXBs quickly rises and then ceases within at most a few decades. If the accretor is a neutron star (NS), and if the accretion outburst is long enough to significantly heat its crust, we speak of a *quasi-persistent transient LMXB*. See Figure 2 for a schematic representation of the interior of a neutron star.²

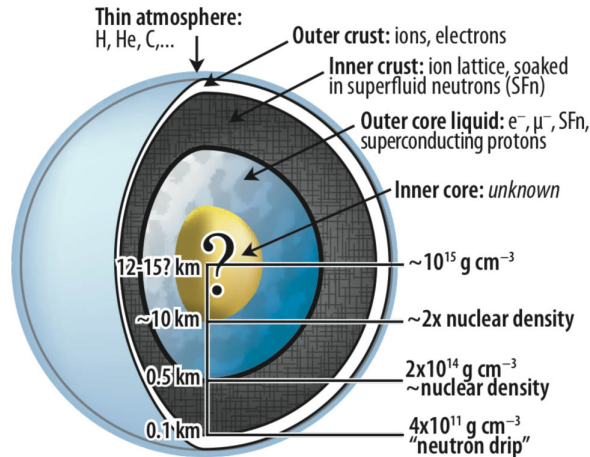


Figure 2: Schematic representation of a neutron star interior

This last subclass of LMXBs is particularly interesting, because when the accretion phase of a quasi-persistent transient ends, the NS crust is no longer in thermal equilibrium with the NS atmosphere and core. The heat gained during accretion (through a process called *deep crustal heating*, see e.g. Brown and Cumming, 2009) is lost during the *quiescent* episode that follows, resulting in *thermal* emission from the NS surface. If a reliable distance estimate is available, fitting this emission with NS atmosphere models allows us to deduce properties of the neutron star, most notably its mass and its radius. This gains us insight into the *equation of state* (EoS, i.e. the mathematical description of the relations between the temperature, pressure and density of matter) of neutron stars and, consequently, into their internal composition. As neutron stars are the most compact physical objects in the present Universe, they form a unique laboratory to study the physics of matter at extreme densities (up to $10^{15} \text{ g cm}^{-3}$, about ten times the density of an atomic nucleus) and to test general relativity in extreme conditions. Furthermore, inferring the EoS of cold, dense nuclear matter is paramount to modelling supernova explosions, gamma-ray bursts and gravitational waves emitted by merging neutron stars.

²Picture taken from NASA's High Energy Astrophysics Science Archive Research Center (HEASARC) website

This thesis will focus on the neutron star LMXB EXO 0748-676, one of the most interesting quasi-persistent transients observed to date. It was discovered with EXOSAT in 1984 (Parmar et al., 1986). It started a transition from outburst to quiescence in August 2008, after more than 24 years of continuous accretion (Díaz Trigo et al., 2011). Galloway et al. (2008b) estimated the distance of EXO 0748-676 to be 7.1 ± 1.2 kpc. Cottam et al. (2002) reported a gravitational redshift of $z_g = 0.35$ at the star’s surface. I will try to compute, or at least constrain, the mass and radius of EXO 0748-676 to provide a constraint on the equation of state of dense nuclear matter. I will do this by fitting theoretical models to X-ray spectra obtained with the XMM-Newton observatory. In Section 2, I will describe the observations and the data reduction. In Section 3, I will elaborate on the process of defining models and fitting them to the data. In Section 4, I will show the results. In Section 5, I will discuss the results. In Section 6, I will conclude my thesis.

2 OBSERVATIONS

2.1 XMM-Newton instruments

The XMM-Newton (X-ray Multi-Mirror Mission) spacecraft is the largest scientific satellite ever launched by the European Space Agency. It was launched in December 1999 into a highly eccentric orbit with a ~ 48 hour period. The satellite includes three 1500 cm^2 telescopes, each with an X-ray detector at their focus. It is composed of four main elements, see Figure 3.³

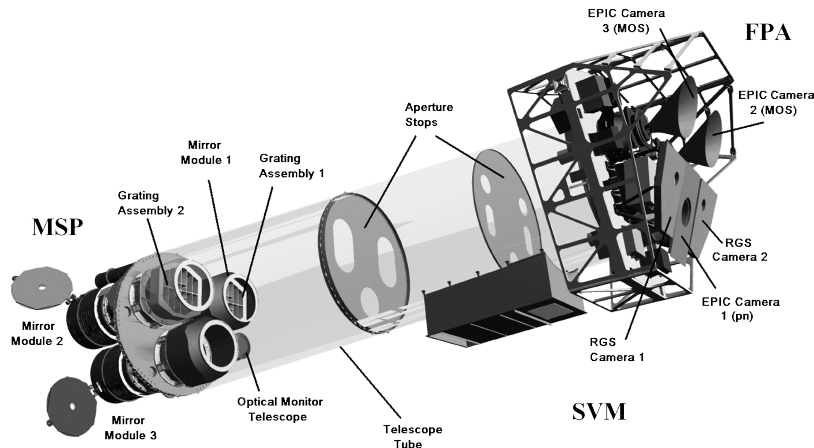


Figure 3: Schematic illustration of the XMM-Newton spacecraft

These elements are:

- The Focal Plane Assembly (FPA), containing the Focal Plane Platform, which carries the focal-plane instruments: two 0.33-2.5 keV Reflection Grating Spectrometers (RGS) readout cameras and a set of three 0.15-15 keV charge-coupled device (CCD) cameras, comprising the European Photon Imaging Camera (EPIC). It also contains the cameras’ data handling, power distribution and cooling units.
- The Mirror Support Platform (MSP), which carries the mirror modules, mirror doors and the two RGS grating boxes. It also contains the 170-650 nm Optical Monitor, which provides simultaneous coverage with the X-ray instruments, and two star-trackers.
- The Telescope Tube, maintaining the relative position between the FPA and the MSP
- The Service Module (SVM), carrying the spacecraft subsystems and associated units. Also attached to the SVM are two solar-array wings and the Telescope Sun Shield.

³Picture taken from the SPIE digital library

In this thesis, I will only analyse data from the three EPIC detectors. One of these uses an array of pn CCDs (Strüder et al., 2001), while the other two use an array of MOS (metal-oxide semiconductor) CCDs (Turner et al., 2001). There are seven CCDs in the focal plane of each MOS camera, designed to approximately follow the focal plane curvature, while the pn camera contains twelve CCDs on a single wafer, see Figure 4.⁴ The RGS gratings divert part of the telescope incident flux towards the RGS detectors, such that about 44% of the original incoming flux reaches the MOS cameras. The telescope with the pn camera has an unobstructed beam.

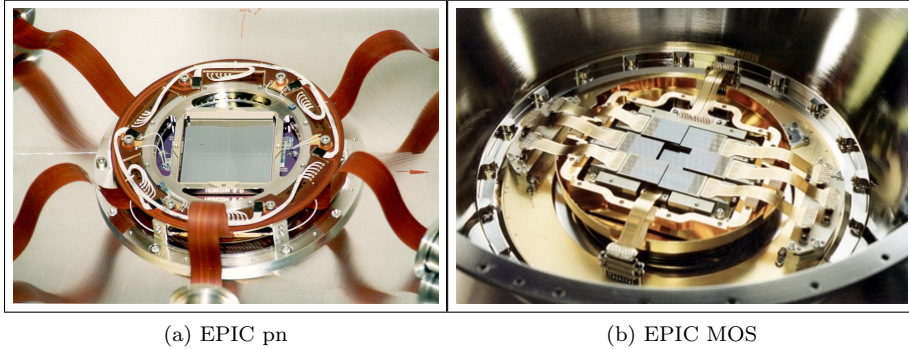


Figure 4: The CCDs of the EPIC imaging detectors

The EPIC cameras offer the possibility to perform extremely sensitive imaging observations with moderate spectral ($E/\Delta E \sim 20\text{-}50$) and angular resolution. All EPIC CCDs operate in photon counting mode with a fixed, mode dependent frame read-out frequency, producing event lists: tables with one entry line per received event (i.e. the detection of one or more photons), listing attributes such as the position at which they were registered, their arrival time and their energies.

2.2 XMM-Newton observations

Table 1. XMM-Newton observations of EXO 0748-676 since March 2009

Observation ID	Date	Instrument	T [ks]	C [s ⁻¹]
0605560401	2009 March 18	pn	36	0.479 ± 0.004
		MOS1	42	0.096 ± 0.002
		MOS2	41	0.118 ± 0.002
0605560501	2009 July 1	pn	86	0.417 ± 0.002
		MOS1	100	0.102 ± 0.001
		MOS2	100	0.102 ± 0.001
0651690101	2010 June 17 (05:32:53)	pn	25	0.406 ± 0.003
		MOS1	30	0.102 ± 0.001
		MOS2	30	0.096 ± 0.001
0651690101	2010 June 17 (15:20:42)	pn	59	0.404 ± 0.004
		MOS1	67	0.101 ± 0.002
		MOS2	67	0.100 ± 0.002
0690330101	2013 April 15	pn	91	0.347 ± 0.002
		MOS1	103	0.064 ± 0.001
		MOS2	103	0.083 ± 0.001

Notes. T is the net exposure time and C the 0.2-10 keV source persistent net count rate. In all cases, the full frame mode with the thin filter was used for all EPIC cameras.

⁴Pictures taken from the European Space Agency website

Table 1 is a summary of the XMM-Newton observations reported in this thesis. All the observations were performed using the EPIC full frame mode. In this mode, all pixels of all CCDs are read out and thus the full field of view (30 arcminutes) is covered; the pn (MOS) CCDs are read out once every 73.4 ms (2.6 s). The source count rate is well below the (point source) threshold of 2 (0.5) s^{-1} , where pile-up effects become important for the pn (MOS) cameras. Photon pile-up is the arrival of more than one X-ray photon in one camera pixel or in adjacent pixels before it is read out. This can affect both the point spread function (PSF) and the spectral response of EPIC, because the onboard event reconstruction software (which suppresses large events, such as induced by most cosmic rays) rejects multi-pixel photon patterns.

For some reason, the third observation turned out to be divided into two segments. I will handle this by treating these segments as two separate observations, but with all of their model parameters tied (see Section 3), because the properties of neutron stars do not change significantly within the timeframe of a mere few hours.

2.3 Data reduction

The observations mentioned above resulted in fifteen discrete X-ray spectra, which consist of a number of energy bins, called *channels*, with each channel containing a certain number of photon counts. The spectra were provided to me by my supervisor, so I did not have to do any of the data reduction and calibration myself. The data products were reduced using the Science Analysis Software (SAS) version 14.0.0. Source events were extracted from a circle centered on the PSF core, and background events from a circle centered well away from the source. Response matrices and ancillary response files were created using the SAS tasks *rmfgen* and *arfgen*, respectively. The times of eclipses (i.e. when one star passes in front of the other, decreasing the flux) were excluded from the spectra, and the spectra were rebinned to have a minimum of 25 counts per bin, to allow the use of the χ^2 statistic (see Section 3). Further details can be found in Díaz Trigo et al. (2011).

This data reduction process resulted in four FITS (Flexible Image Transport System) files per spectrum: the spectrum itself, the background spectrum, the response matrix and an ancillary response file. All this is explained in Appendix A. The only thing I still had to do, was to remove all data outside of the 0.2-10 keV range (below 0.2 keV the data are not calibrated; above 10 keV the source does no longer emit), plus any additional channels labeled as ‘bad’, for whatever reason, in the headers of the spectral files. The final spectra, including error bars, can be seen in Figure 5. Of the third observation, only the first segment is shown. Of the MOS spectra, only those of the first MOS camera are shown.

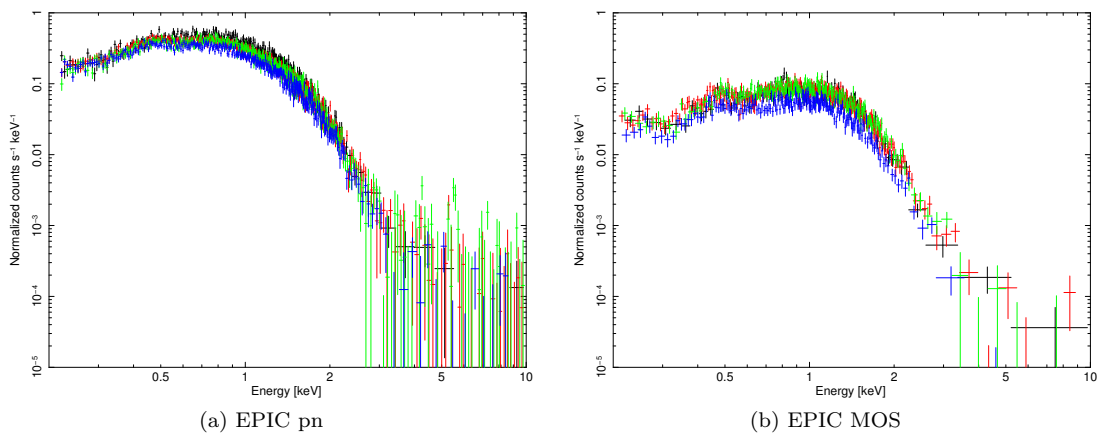


Figure 5: X-ray spectra. Observations 1-4 are shown in black, red, green and blue, respectively.

3 DATA ANALYSIS

3.1 Defining model spectra

I have used XSPEC (Arnaud, 1996) version 12.8.2 to analyse the resulting X-ray spectra. XSPEC is an X-ray spectral fitting package that contains an extensive library of theoretical models. There are two basic kinds of model components: *additive* components, which represent X-ray sources of different kinds, and *multiplicative* components, which represent phenomena that modify the observed X-ray radiation. Since there must be a source, there must be at least one additive component in a model, but there is no restriction on the number of modifying components. Model components are described in terms of a few parameters. For example, a blackbody (*bbody* in XSPEC) is described in terms of a temperature and a normalisation.

Once a model has been defined, XSPEC can try to fit the model to the data by running a numerical fitting algorithm. This algorithm (an implementation of the Levenberg-Marquadt algorithm) varies the model parameters until the *fit statistic* has reached a desirable value. The most commonly used fit statistic is χ^2 , which has to be minimised in order to find the best-fit parameters. Once the fitting procedure is completed, XSPEC writes out a list of the best-fit parameter values, as well as the corresponding χ^2 . How good the fit *really* is, however, also depends on the number of degrees of freedom ν , which is defined as the number of channels minus the number of independent model parameters. As a general rule, one wants the ‘reduced χ^2 ’ ($\chi_\nu^2 = \chi^2/\nu$) to be approximately equal to one. Even then, one can still not say that the model is acceptable. The parameter values have to be physical (see, for example, Section 5.2), and there could be many different models that yield fits that are just as good, or perhaps even better. In the end, picking the correct model is a matter of scientific judgement. For a comprehensive overview of spectral fitting with XSPEC, including the definition of χ^2 and a list of assumptions made by using this fit statistic, see Appendix A.

Deciding which model to use is not an easy task. There is a plethora of model components available, and they can be combined in infinitely many ways. Fortunately, there are a few factors that limit the amount of viable options. These are, for example, the shape of the extracted X-ray spectra (see Figure 5), as well as the results of earlier studies on EXO 0748-676 (e.g. Díaz Trigo et al., 2011). Yet, I will be careful not to let the latter affect my own results too much, as I do not strive to merely copy the work of others. After all, the nature of EXO 0748-676 is not yet completely understood, and many of its properties are still open to interpretation and debate. For this reason, I started out by defining and fitting a set of *sixteen* different models. They are similar in the sense that they are all combinations of the few model components that I have deemed ‘viable’, but apart from that, I have tried to keep all options open.

The abovementioned ‘limiting factors’ led me to believe that all models should probably contain a *thermal* component, like a blackbody component or a neutron star atmosphere model (i.e. a modified blackbody), possibly accompanied by another additive component to account for any additional features. Furthermore, since neutron stars in LMXBs do not display evidence of a strong magnetic field (Díaz Trigo et al., 2011), I have decided to use ‘non-magnetic’ ($B \leq 10^8$ G) NS atmosphere models only. What is more, I have included some form of interstellar absorption in every model. Lastly, I have included constant factors, fixed to one for the EPIC pn spectra but allowed to vary for the EPIC MOS spectra, to account for cross-calibration uncertainties.

ADDITIVE MODEL COMPONENTS

- *bbody*: a blackbody spectrum. A blackbody is an idealised physical body that absorbs all incident electromagnetic radiation. A blackbody in thermal equilibrium emits radiation according to Planck’s law, meaning that it has a spectrum that is determined by temperature alone. Hence, *bbody* is defined in terms of the blackbody’s ‘temperature’ in keV (= kT) and a normalisation that depends on both its luminosity and its distance.

- *bbodyrad*: another blackbody spectrum. The only difference lies in the fact that *bbodyrad*'s normalisation is proportional to the *surface area* of the source, rather than to its *luminosity*. The two blackbody components should yield identical results.
- *compTT*: a thermal Comptonisation component (Titarchuk, 1994). Comptonisation (or: *inverse Compton scattering*) is the upscattering of soft (i.e. low-energy) photons by a charged particle, usually an electron. *compTT* does not care whether these photons originate from the neutron star itself or from a (residual) accretion disc, but it is unlikely that this source is still accreting (Díaz Trigo et al., 2011). At high temperatures, the effectiveness of the Comptonisation process increases substantially: $E_e \sim \frac{3}{2}kT_e$. *compTT* is defined in terms of redshift, soft photon temperature, plasma temperature, plasma optical depth, geometry (spherical or disc) and a normalisation. The spectrum it produces resembles a power law.
- *nsatmos*: a NS hydrogen atmosphere model (Heinke et al., 2006). Atmosphere models are constructed by solving the (one-dimensional) radiative transfer equation, and the atmosphere is assumed to be in radiative and hydrostatic equilibrium. This particular model interpolates from a grid of NS atmosphere calculations to output a NS atmosphere spectrum. The model grids cover a wide range of surface gravity (see Section 4.2) and effective temperature, and incorporate thermal electron conduction and self-irradiation by photons from the compact object. It is noted that the neglect of neutral hydrogen limits the validity of the code to temperatures $T_{eff} \geq 3 \times 10^5$ K, while the omission of Comptonisation limits it to perhaps $T_{eff} \leq 3 \times 10^6$ K. (Zavlin et al., 1996) *nsatmos* is defined in terms of unredshifted effective (surface) temperature, neutron star gravitational mass, ‘true’ neutron star radius, distance and a normalisation. For this model, the normalisation is given by the fraction of the neutron star surface that is emitting. The effective (surface) temperature of a star is defined as the temperature a blackbody would have if it were to emit the same total flux of electromagnetic energy. *Unredshifted* effective temperature and *true* neutron star radius refer to physical quantities as ‘measured’ in the NS frame of reference. This implies that their XSPEC values are not what a distant observer would measure (‘values at infinity’). General relativistic effects might come into play. In that case, $T_{eff}^\infty = T_{eff}/(1+z_g)$ and $R^\infty = R(1+z_g)$, where z_g is the gravitational redshift. R^∞ is known as the *radiation radius*.
- *nsagrav*: another NS hydrogen atmosphere model (Zavlin et al., 1996). This model is similar to *nsatmos* in many respects. The main differences are its smaller effective temperature, mass and radius ranges, and the fact that it does not allow you to specify the fraction of the neutron star surface that is emitting. Instead, its normalisation is given by one over the distance in parsecs squared. As for the rest of the parameters, they are exactly the same. This does not mean, however, that the *models* are exactly the same. They are *similar*, but this does not guarantee that they will also yield similar results. Small differences in assumptions made, opacity tables used, physical processes accounted for, et cetera, could potentially have a large impact on (some of) the best-fit parameters.
- *nsx*: a NS helium atmosphere model (Ho and Heinke, 2009). This model is also much alike the previous two. It interpolates from a grid of NS atmosphere spectra to produce a final spectrum that depends on the same parameters as *nsatmos*. Nonetheless, this model sets itself apart by assuming that the NS atmosphere is composed of *helium*. In fact, *nsx* allows one to set the chemical composition to either helium or carbon, but I will not use the latter. If there is accretion after neutron star formation, its atmosphere could be composed of light elements (H or He). If no accretion takes place, or if the light elements are dragged down by convection or burned in thermonuclear reactions, heavy elements (e.g. Fe) are expected. Because neutron stars in quiescent LMXBs have *just* passed through an accretion stage, it is safe to assume that EXO 0748-676’s atmosphere is either hydrogen-dominated or helium-dominated. It has been suggested that the short rise-times and short duration of three photospheric radius expansion bursts, detected in May 2004 and June and August 2005, indicate ignition in a He-rich environment (Galloway et al., 2008a).

- *powerlaw*: a simple photon power law of the form $KE^{-\alpha}$. Evidently, *powerlaw* is defined in terms of dimensionless photon index α and a normalisation K . For this component, the normalisation is given by the amount of photons $\text{keV}^{-1} \text{cm}^{-2} \text{s}^{-1}$ (i.e. the flux density) at 1 keV. Even if the addition of this component were to provide an adequate fit, its origin would still be up for interpretation. There are many phenomena that give rise to a power law spectrum. It has been suggested that such a feature might be caused by a shock from a pulsar wind, or by residual low-level accretion onto the magnetosphere, although the latter is deemed unlikely (Díaz Trigo et al., 2011).

MULTIPLICATIVE MODEL COMPONENTS

- *constant*: an energy-independent multiplicative factor. This component is used to account for cross-calibration uncertainties and will therefore be incorporated into every model. It corrects for the fact that all XMM-Newton instruments are calibrated independently. Even though great care has been taken in defining standards and procedures for high energy calibration, the calibration of the different instruments will never be *exactly* equal. Freezing this factor to one for the EPIC pn spectra, while allowing it to vary for the EPIC MOS spectra, allows XSPEC to adjust their *relative* calibration if needed. If it results in a better fit, that is. This makes these factors just another parameter to fit. Since the cross-calibration errors are expected to be small, the *constant* factors should all be close to unity.
- *phabs*: X-ray photoelectric absorption. This interstellar absorption component uses cross-sections set by the XSPEC command *xsect* and relative (with respect to hydrogen) *solar* abundances set by the XSPEC command *abund*:

$$M(E) = e^{-N_H \sigma(E)},$$

where $M(E)$ is the ensuing energy-dependent multiplicative factor, N_H is the equivalent column number density of the interstellar hydrogen (in units of $10^{22} \text{atoms cm}^{-2}$), and $\sigma(E)$ is the total cross-section of the interstellar medium (ISM), *not* including Thomson scattering:

$$\sigma(E) = \sum_i \frac{N_i}{N_H} \sigma_i(E) = \frac{N_H}{N_H} \sigma_H(E) + \frac{N_{He}}{N_H} \sigma_{He}(E) + \dots + \frac{N_{Ni}}{N_H} \sigma_{Ni}(E),$$

where the summation is over atomic species i . The abundance tables all contain the measured solar abundances of all the elements ranging from hydrogen ($Z = 1$) to zinc ($Z = 30$). The cross-section tables contain the laboratory-measured photoionisation cross-sections of eighteen astrophysically important elements ranging from hydrogen ($Z = 1$) to nickel ($Z = 28$). Hence, there will be eighteen contributions to the total cross-section. What contributions exactly depends on the table used. It is assumed that the solar abundance vector is a good approximation of the ISM abundance vector. Although the amount of X-ray extinction is generally expressed in terms of the equivalent hydrogen column density, it is generally caused by the most abundant heavier elements like O, Ne, Fe, Mg and Si (Güver and Özel, 2009). The default options for *xsect* and *abund* are *bcmc* (Balucinska-Church and McCammon, 1992; Yan et al., 1998) and *angr* (Anders and Grevesse, 1989), respectively. I will not change these defaults. With *xsect* and *abund* specified, the only actual *phabs* parameter is N_H .

- *tbabs*: X-ray absorption. This interstellar absorption component is a considerably more complicated version of *phabs*. It does not only take the gas-phase ISM into account, but also the grain-phase ISM and the molecular hydrogen in the ISM. It also considers the effect of shielding by dust grains, as well as the depletion of gas onto dust grains. Furthermore, it makes use of updated photoelectric absorption cross-section and abundance tables. In XSPEC, these tables are called *vern* (Verner et al., 1996) and *wilm* (Wilms et al., 2000), respectively. This component is expected to yield better results than *phabs*, but to take a lot more time in doing so.

3.2 Fitting model spectra

Table 2 is a summary of my first attempts at creating a model whose predicted spectra closely resemble the observed spectra. To obtain the tightest possible constraints on the mass and the radius of the neutron star, I fitted all fifteen data sets simultaneously.

Table 2. Initial attempts at defining a well fitting model

#	Model	χ^2_ν (d.o.f.)	Null hypothesis probability
1	<i>phabs * nsatmos</i>	1.07537 (3698)	7.60998e-04
2	<i>tbabs * nsatmos</i>	1.06469 (3698)	3.15155e-03
3	<i>phabs * (nsatmos + powerlaw)</i>	1.05798 (3693)	7.08937e-03
4	<i>tbabs * (nsatmos + powerlaw)</i>	1.04571 (3693)	2.60315e-02
5	<i>tbabs * nsagrav</i>	1.06353 (3698)	3.64066e-03
6	<i>tbabs * nsx</i>	1.04514 (3698)	2.74040e-02
7	<i>tbabs * (nsagrav + powerlaw)</i>	1.04152 (3693)	3.31245e-01
8	<i>tbabs * (nsx + powerlaw)</i>	1.02437 (3693)	1.47630e-01
9	<i>tbabs * (nsatmos + compTT)</i>	1.01002 (3685)	3.31245e-01
10	<i>tbabs * (nsagrav + compTT)</i>	1.00838 (3685)	3.57075e-01
11	<i>tbabs * (nsx + compTT)</i>	1.01313 (3685)	2.84773e-01
12	<i>tbabs * bbody</i>	1.29284 (3696)	4.026851e-31
13	<i>tbabs * powerlaw</i>	1.59195 (3699)	1.55518e-104
14	<i>tbabs * (bbody + powerlaw)</i>	1.59971 (3691)	1.21305e-106
15	<i>tbabs * (bbodyrad + powerlaw)</i>	1.59411 (3694)	4.81094e-105
16	<i>tbabs * (powerlaw + powerlaw)</i>	1.55838 (3694)	1.53795e-94

Notes. χ^2_ν is the reduced χ^2 and d.o.f. the number of degrees of freedom (see text). The null hypothesis probability is the probability of getting a value of χ^2 as large or larger than observed if the model is correct. If this probability is small, the model is not a good fit.

To obtain these values, I first used the XSPEC command *model*. For all models, I fixed the distance to the best-fit distance found by Galloway et al. (2008b), namely 7.1 kpc. Because I assume the neutron star to be ‘non-magnetic’, I fixed the normalisation of *nsatmos* and *nsx* to 1, corresponding to the entire NS surface emitting. I fixed the normalisation of *nsagrav*, which is defined as one over the distance in parsecs squared, to $1/7100^2 = 1.98373 \times 10^8$. Furthermore, I assumed that the mass and radius of the neutron star, as well as the value of N_H , do not change significantly among observations, so I tied these parameters for the different data groups. The only parameters that might change, are those that depend on temperature (since the system is cooling), or those that do not depend on the properties of the neutron star (e.g. the normalisation of the power law component), so I allowed these to vary from one observation to the next. I then used the XSPEC command *fit* to carry out the fitting procedure.

As mentioned previously, a χ^2_ν close to unity indicates a good fit. From this, I quickly concluded that *tbabs* yields better results than *phabs* (as expected), so I stopped using *phabs*. All moderately good fits stem from models that contain an NS atmosphere model, which is also not surprising. What *is* surprising, is that the best fits are produced by the models that also include a power law or a thermal Comptonisation component. Upon closer inspection, however, the best-fit parameters of these models did not turn out to be physical. As can be seen in Figure 6, these components merely contribute to the low-energy end of the spectrum, while the process of inverse Compton scattering *should* give to a high-energy ‘tail’. Furthermore, the documentation of the *compTT* component states that it is not valid for simultaneously low (soft photon) temperatures and low plasma optical depth, which is also the case here.

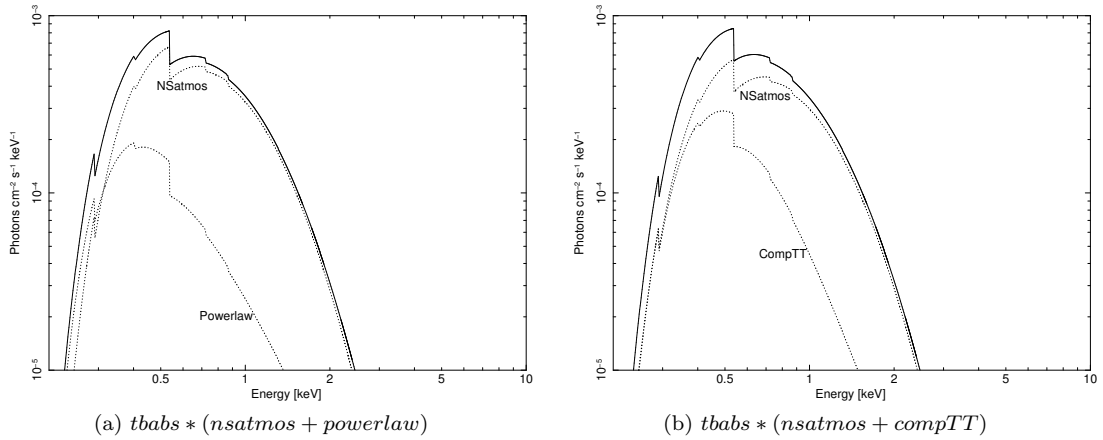


Figure 6: The contribution of the power law and Comptonisation components, respectively, to one of the model spectra. The dotted lines show the individual contributions of the (absorbed) additive model components. The solid line shows the total model spectrum.

This leaves us with $tbabs * nsatmos$, $tbabs * nsagraw$ and $tbabs * nsx$, with χ^2_ν -values of 1.06469, 1.06353 and 1.04514, respectively. The helium atmosphere model yields slightly better results than the two hydrogen atmosphere models, but with a null hypothesis probability of at most 2.74%, none of the models fit particularly well. Perhaps the shape of the residuals might give a clue to what is missing, see Figure 7(a). Unfortunately, the sheer number of data points obscures the shape. Therefore, I used the XSPEC command `setplot rebin` to combine each eight adjacent bins into one, see Figure 7(b). This time, a clear wave-like pattern emerges. This means that an extra additive model component might improve the fit. A gaussian line profile (`gaussian` in XSPEC), centered at the first maximum of the ‘wave’, should be able to reduce the residuals considerably.

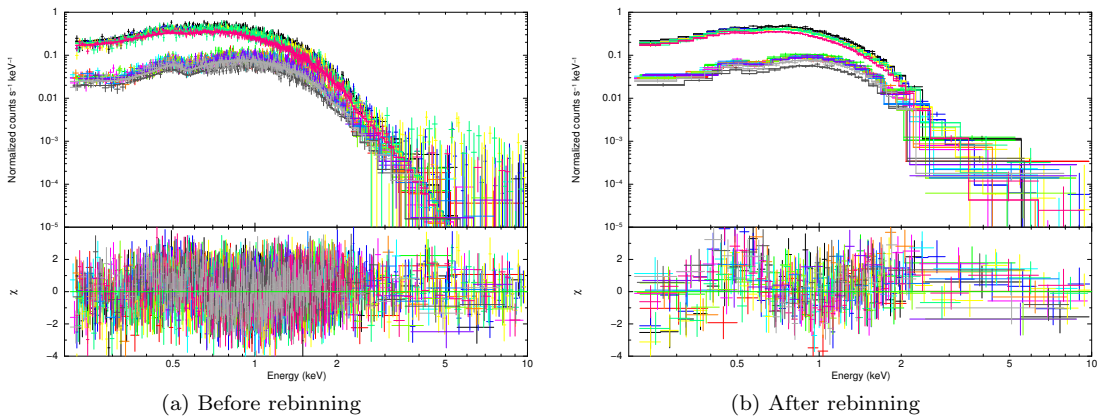


Figure 7: Data, folded model and residuals for the $tbabs * nsatmos$ model. The wave-like structure indicates that the residuals are not just random ‘noise’.

This *gaussian* component can be understood as an emission line, although other explanations also exist, see Section 5.3. It is defined in terms of line energy, line width and a normalisation. I tied the energy and width for all the observations, but I allowed the normalisation to vary. As expected, the ensuing models yield good results, which the remaining sections will discuss extensively.

4 RESULTS

4.1 Best-fit models

Tables 3-5 show the results of the best-fit models, $tbabs*(nsatmos + gaussian)$, $tbabs*(nsagrav + gaussian)$ and $tbabs*(nsx + gaussian)$, respectively, for a distance of 7.1 kpc. The fits are acceptable, with a χ^2_ν of 1.01 for 3692 degrees of freedom. All uncertainties are given at 90% confidence ($\Delta\chi^2 = 2.71$ for one interesting parameter, see Appendix A). I used the XSPEC command *error* to compute most of the confidence intervals. For those of kT_{eff}^∞ and the fluxes, I had to use a different method, which is explained in Appendix B. Unfortunately, this drove the uncertainties in these parameters to unrealistically large values.

Table 3. Best-fits to the 0.2-10 keV EPIC spectra for all the observations simultaneously with the $tbabs*(nsatmos + gaussian)$ model

Observation	N_H [10^{21} cm^{-2}]	kT_{eff}^∞ [eV]	M [M_\odot]	R [km]	F_{tot}	F_{NS}	χ^2_ν (d.o.f.)
0605560401	$0.91^{+0.10}_{-0.13}$	111^{+19}_{-19}	$2.37^{+0.07}_{-0.17}$	$12.1^{+1.6}_{-1.8}$	$1.2^{+1.0}_{-0.7}$	$1.1^{+0.6}_{-0.7}$	1.01 (3692)
0605560501		107^{+18}_{-19}			$1.1^{+0.9}_{-0.6}$	$0.9^{+0.9}_{-0.6}$	
0651690101		107^{+18}_{-19}			$1.0^{+0.8}_{-0.6}$	$0.9^{+0.8}_{-0.6}$	
0690330101		103^{+17}_{-18}			$0.9^{+0.7}_{-0.5}$	$0.8^{+0.7}_{-0.5}$	

Notes. F_{tot} and F_{NS} are the 0.2-10 keV total and neutron star unabsorbed fluxes in units of $10^{-12} \text{ erg cm}^{-2} \text{ s}^{-1}$. The remaining flux comes from the gaussian line component, see Section 4.3. During the fits, the distance was fixed to 7.1 kpc and the *nsatmos* normalisation to 1 (see text).

Table 4. Best-fits to the 0.2-10 keV EPIC spectra for all the observations simultaneously with the $tbabs*(nsagrav + gaussian)$ model

Observation	N_H [10^{21} cm^{-2}]	kT_{eff}^∞ [eV]	M [M_\odot]	R [km]	F_{tot}	F_{NS}	χ^2_ν (d.o.f.)
0605560401	$0.93^{+0.12}_{-0.15}$	111^{+35}_{-30}	$1.91^{+0.59}_{-1.61}$	$14.6^{+1.5}_{-0.9}$	$1.2^{+2.0}_{-0.8}$	$1.1^{+2.0}_{-0.8}$	1.01 (3692)
0605560501		107^{+42}_{-28}			$1.1^{+2.5}_{-0.6}$	$0.9^{+2.5}_{-0.6}$	
0651690101		107^{+40}_{-28}			$1.0^{+2.3}_{-0.6}$	$0.9^{+2.3}_{-0.6}$	
0690330101		103^{+38}_{-28}			$0.9^{+1.9}_{-0.6}$	$0.8^{+1.9}_{-0.6}$	

Notes. See the notes of Table 3 for definitions. During the fits, the *nsagrav* normalisation was fixed to 1.98373×10^8 (see text). The mass is not constrained, see Section 4.2.

Table 5. Best-fits to the 0.2-10 keV EPIC spectra for all the observations simultaneously with the $tbabs*(nsx + gaussian)$ model

Observation	N_H [10^{21} cm^{-2}]	kT_{eff}^∞ [eV]	M [M_\odot]	R [km]	F_{tot}	F_{NS}	χ^2_ν (d.o.f.)
0605560401	$0.91^{+0.09}_{-0.06}$	99^{+20}_{-20}	$2.83^{+0.17}_{-0.77}$	$17.9^{+2.8}_{-3.4}$	$1.2^{+1.3}_{-0.8}$	$1.2^{+1.3}_{-0.8}$	1.01 (3692)
0605560501		96^{+19}_{-20}			$1.1^{+1.2}_{-0.7}$	$1.0^{+1.2}_{-0.7}$	
0651690101		96^{+19}_{-20}			$1.0^{+1.2}_{-0.7}$	$1.0^{+1.2}_{-0.7}$	
0690330101		92^{+19}_{-19}			$0.9^{+1.0}_{-0.6}$	$0.9^{+1.0}_{-0.6}$	

Notes. See the notes of Table 3 for definitions. During the fits, the distance was fixed to 7.1 kpc, the *nsx* normalisation was fixed to 1, and the *specfile* parameter was fixed to 2, indicating a helium atmosphere. The mass is not bounded from above, see Section 4.2.

4.2 Contour plots

Because my main interest lies in determining the neutron star’s mass and radius, I have further investigated these parameters with the help of the XSPEC command *steppar*. This command runs a grid over two parameters. At each point in the grid, XSPEC fixes the two parameters and refits the rest of the model. When this procedure is finished, a built-in interpolation routine can transform the discrete set of χ^2 -values to a *contour plot*, which shows two-dimensional confidence intervals. By default, the 68%, 90% and 99% probability contours are shown, corresponding to a $\Delta\chi^2$ of 2.30, 4.61 and 9.21, respectively, see Appendix A. Figures 8-10 show the resulting contour plots for each of the best-fit models, using a 32×32 *steppar* grid. The fact that none of the contour lines are circular indicates that the parameters are correlated. The figures also show the regions for which the models are defined or, rather, for which they are *not*. In practice, NS atmosphere models are only defined for a certain range of parameter values. Most notably, the model grids are defined for a certain range of *surface gravity*, g , which depends on the neutron star mass M and radius R and plays an important role in spectral fitting (Heinke et al., 2006). It is given by:

$$g = \frac{1}{g_r} \frac{G}{MR^2},$$

where g_r is the *redshift parameter*,

$$g_r = \frac{1}{1 + z_g} = \sqrt{1 - \frac{r_s}{R}} = \sqrt{1 - \frac{2GM}{c^2 R}}$$

and $r_s = 2GM/c^2$ is the *Schwarzschild radius*. *nsatmos*, *nsagrav* and *nsx* are defined for surface gravities between 10^{11} and 10^{16} cm s^{-2} , between 10^{13} and 10^{15} cm s^{-2} , and between $10^{13.6}$ and $10^{14.9}$ cm s^{-2} , respectively. Furthermore, *nsagrav* is only defined for $g_r^2 > 1/3$. Although these boundaries might seem random, the allowed domain in the M-R plane is also restricted for physical reasons, see Section 5.2. Figure 11 shows the 99% probability contours of each model.

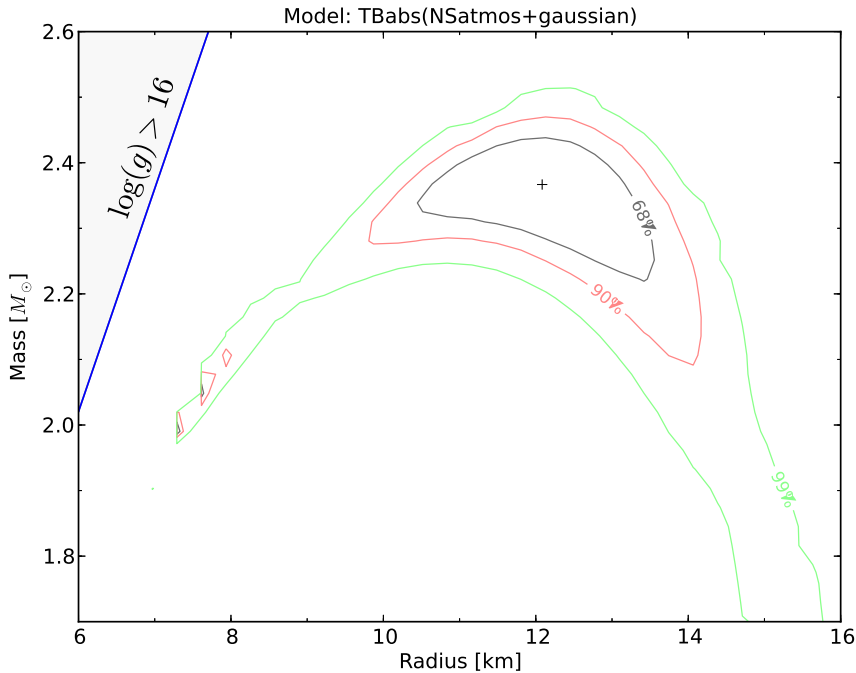


Figure 8: Contour plot for the mass and radius of the NS for the fits shown in Table 3

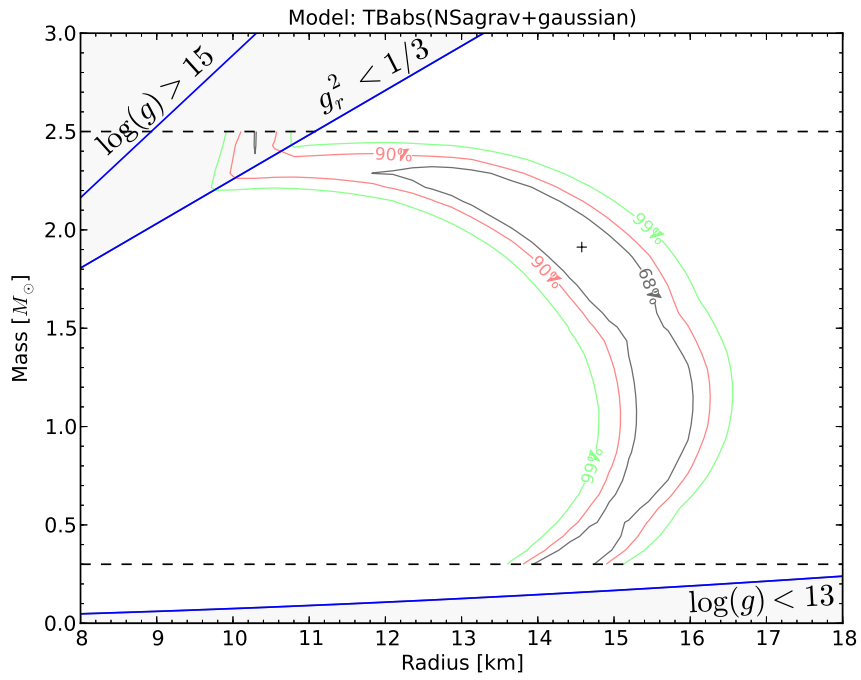


Figure 9: Contour plot for the mass and radius of the NS for the fits shown in Table 4

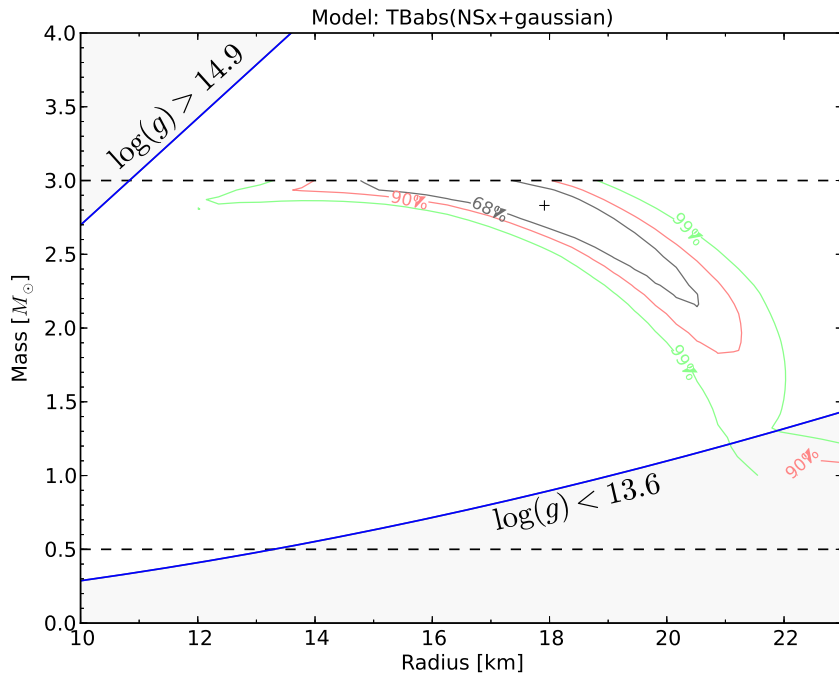


Figure 10: Contour plot for the mass and radius of the NS for the fits shown in Table 5

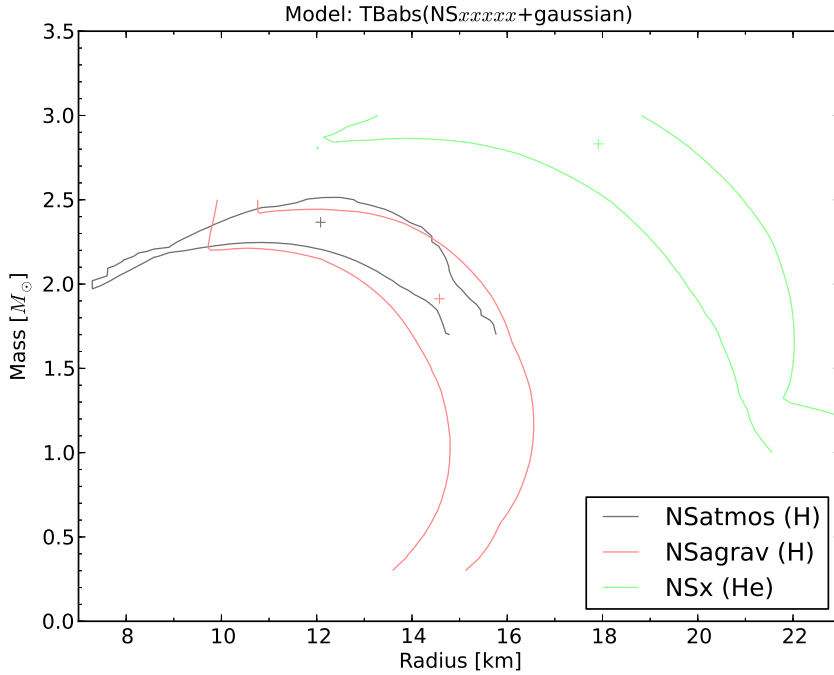


Figure 11: 99% probability contours for each model

4.3 Emission lines

Table 6. Best-fits to the 0.2-10 keV EPIC spectra for all the observations simultaneously with the *tbabs* * (*nsatmos* + *gaussian*) model

Observation	Line energy [keV]	Line width [keV]	K_{gauss}	F_{gauss}	F_{gauss}/F_{tot} [%]
0605560401	$0.36^{+0.13}_{-0.22}$	$0.18^{+0.03}_{-0.08}$	$1.8^{+1.3}_{-1.4}$	0.10	8.5
0605560501			$2.4^{+1.6}_{-1.4}$	0.13	12.2
0651690101			$1.7^{+1.3}_{-1.2}$	0.091	8.9
0690330101			$2.1^{+1.6}_{-1.3}$	0.12	13.0

Notes. K_{gauss} is the normalisation of the gaussian line component in units of 10^{-4} ph. cm $^{-2}$ s $^{-1}$. F_{gauss} is the 0.2-10 keV gaussian unabsorbed flux in units of 10^{-12} erg cm $^{-2}$ s $^{-1}$.

Table 7. Best-fits to the 0.2-10 keV EPIC spectra for all the observations simultaneously with the *tbabs* * (*nsagrav* + *gaussian*) model

Observation	Line energy [keV]	Line width [keV]	K_{gauss}	F_{gauss}	F_{gauss}/F_{tot} [%]
0605560401	$0.32^{+0.16}_{-0.14}$	$0.20^{+0.09}_{-0.09}$	$2.4^{+4.7}_{-1.8}$	0.12	9.9
0605560501			$3.1^{+6.6}_{-2.3}$	0.15	13.7
0651690101			$2.2^{+4.2}_{-1.7}$	0.11	10.3
0690330101			$2.7^{+7.4}_{-2.0}$	0.13	14.5

Notes. See the notes of Table 6 for definitions.

Table 8. Best-fits to the 0.2-10 keV EPIC spectra for all the observations simultaneously with the *tbabs* * (*nsx* + *gaussian*) model

Observation	Line energy [keV]	Line width [keV]	K_{gauss}	F_{gauss}	F_{gauss}/F_{tot} [%]
0605560401	$0.47^{+0.04}_{-0.14}$	$0.12^{+0.08}_{-0.03}$	$0.4^{+1.1}_{-0.3}$	0.028	2.4
0605560501			$0.8^{+1.8}_{-0.3}$	0.058	5.4
0651690101			$0.4^{+1.3}_{-0.2}$	0.027	2.7
0690330101			$0.7^{+1.6}_{-0.3}$	0.054	6.0

Notes. See the notes of Table 6 for definitions.

Tables 6-8 show the remaining results of the best-fit models, namely those related to the gaussian line shape. Its origin is discussed in Section 5.3.

5 DISCUSSION

In short, the results confirm that EXO 0748-676 is a cooling neutron star. The three best-fit models, which all contain a NS atmosphere component, yield continuously decreasing temperatures and (total) fluxes. The equivalent column density of interstellar hydrogen, N_H , is approximately 0.9×10^{21} atoms cm^{-2} for all models, indicating that the absorption component is only weakly model-dependent. The mass and radius of the neutron star, on the other hand, strongly depend on the model chosen. The helium atmosphere model predicts a heavier and larger neutron star than the two hydrogen atmosphere models. None of the models is able to constrain the mass particularly well. For *nsx*, the mass is not bounded from above, and for *nsaggrav*, the mass is not constrained at all. Yet, the contour lines *do* lie within the allowed M-R domains, confirming once again that these models are appropriate. The models yield gaussian lines with slightly different energies and shapes, but since they overlap within their 90% confidence intervals, they might as well be the same. The helium model predicts a slightly weaker line, judging from its smaller line width and lower flux.

5.1 Implications for the accretion rate and efficiency

During the recent accretion phase, EXO 0748-676's neutron star most likely accreted a large amount of matter from its donor. However, not all of the *mass* lost by the donor was transferred to the accretor. Due to viscosity and friction in the accretion disc, and due to the loss of gravitational potential energy during impact, part of it was lost in the form of heat (and eventually radiation). This introduces the so-called *accretion efficiency*, ξ , which is the efficiency of the conversion of the rest mass of the accreted matter into energy (heat). Note that ξ is *not* the efficiency of mass transfer, quite the opposite! We have:

$$\Delta E \propto \Delta mc^2 \implies \Delta E = \xi \Delta mc^2, \quad 0 \leq \xi \leq 1$$

$$L_{bol} = \frac{\Delta E}{\Delta t} = \xi \frac{\Delta m}{\Delta t} c^2 = \xi \dot{m} c^2 \implies \dot{M} = \dot{m} = \frac{L_{bol}}{\xi c^2},$$

where L_{bol} is the average bolometric luminosity of the neutron star during the outburst. $\dot{M} = \dot{m}$, because the mass that is transferred by the infalling material increases the mass of the neutron star. Hence, if one knows L_{bol} and accretion efficiency ξ , one can estimate the *mass accretion rate*, \dot{M} . This rate can then be compared to a different estimate, namely $\dot{M} = \Delta M / \Delta t$, where ΔM is the difference between M_{birth} , usually taken to be the canonical mass of $1.4 M_\odot$, and XSPEC's best-fit value for the neutron star mass, and Δt is the time for which EXO 0748-676 has been accreting. This comparison gives an indication of the feasibility of the neutron star having reached the mass predicted by XSPEC, which might help to pick the (most) correct model.

In principle, I could calculate the bolometric luminosity of the neutron star myself. XSPEC offers this functionality in the form of the *flux* command, in combination with *energies* or *dummyrsp*. This, however, would yield L_{bol} during quiescence, while I need the average L_{bol} during *accretion*. Fortunately, Díaz Trigo et al. (2006) determined the average (0.1-100 keV) thermal bolometric *flux* during accretion to be $1.49 \times 10^{-9} \text{ erg cm}^{-2} \text{ s}^{-1}$. They determined this for the second half of the outburst only, but I will assume that it is a good estimate. I will convert it to a bolometric luminosity by using a luminosity distance, d , of 7.1 kpc,

$$\begin{aligned} L_{bol} &= 4\pi d^2 F_{NS}^{bol} \\ &= 4\pi (7.1 \text{ kpc} \times 3.08567758 \times 10^{21} \frac{\text{cm}}{\text{kpc}})^2 (1.49 \times 10^{-9} \text{ erg cm}^{-2} \text{ s}^{-1}) \\ &= 9.0 \times 10^{36} \text{ erg s}^{-1} \end{aligned}$$

An expression for the accretion efficiency ξ can be obtained by considering matter falling in from infinity, and equating its kinetic and gravitational potential energy. When the matter reaches the surface of the star ($r = R$), part of the kinetic energy of the free-fall is radiated away as heat. This approach neglects energy losses in the accretion disc itself. It yields a ξ of:

$$\begin{aligned} E_T = 0 &\implies E_{KE} = -E_{PE} \implies \frac{1}{2} m v_{ff}^2 = \frac{GMm}{r} \\ L_{bol} &= \frac{dE_{KE}}{dt} = \frac{1}{2} \frac{dm}{dt} v_{ff}^2 = \frac{GM}{R} \frac{dm}{dt} = \frac{GM}{c^2 R} \frac{dm}{dt} c^2 \\ L_{bol} &= \xi \frac{dm}{dt} c^2 \implies \xi = \frac{GM}{c^2 R} = \frac{1}{2} \frac{r_s}{R}, \end{aligned}$$

which scales as M_{NS}/R_{NS} , indicating that the accretion efficiency simply depends on how compact the star is. As the compactness of neutron stars is exceptionally high, so is their accretion efficiency: about 10%, over an order of magnitude larger than the energy conversion efficiency of hydrogen fusion, which releases only about 0.7% of rest mass. To estimate the mass accretion rates, I will assume that EXO 0748-676 was ‘born’ with a mass of $1.4 M_{\odot}$, that it reached its current mass by continuously accreting for exactly 24 years, and that its compactness did not change during the accretion phase. Summarising all of the above, the two estimates are:

$$\begin{aligned} (1) \dot{M} &= \frac{L_{bol}}{\xi c^2} = \frac{\ell^2 R}{GM} \frac{L_{bol}}{\ell^2} = \frac{L_{bol}}{G} \frac{R}{M} \\ (2) \dot{M} &= \frac{\Delta M}{\Delta t}, \end{aligned}$$

for which the different models yield,

- *nsatmos*: $M = 2.37 M_{\odot}$ and $R = 12.1 \text{ km}$, resulting in 3.5×10^{16} and $2.5 \times 10^{24} \text{ g s}^{-1}$, respectively
- *nsagrav*: $M = 1.91 M_{\odot}$ and $R = 14.6 \text{ km}$, resulting in 5.2×10^{16} and $1.3 \times 10^{24} \text{ g s}^{-1}$, respectively
- *nsx*: $M = 2.83 M_{\odot}$ and $R = 17.9 \text{ km}$, resulting in 4.3×10^{16} and $3.8 \times 10^{24} \text{ g s}^{-1}$, respectively

Evidently, the values all differ by *eight* orders of magnitude. Maybe EXO 0748-676 was ‘born’ with a far higher mass, maybe this accretion phase was only one of several, maybe the accretion efficiency is a lot lower than expected (e.g. due to energy losses in the accretion disc), maybe I made wrong assumptions, et cetera. Most likely, it is a combination of the above. Whatever the reason, this method does not enable me to constrain the composition of neutron stars.

5.2 Constraints on the dense matter equation of state

The main goal of this thesis is to constrain the equation of state of cold, dense nuclear matter and thereby gain insight into the internal composition of neutron stars. Their immense gravity leads to strong compression and non-ideality of atmospheric matter, which considerably affects the EoS. Now that the spectral fitting results are in, I can compare contour plots of the mass and radius (see Section 4.2) to theoretical predictions, and see where they overlap. First, I will explain why some regions of the mass-radius plane have to be excluded from the results.

There are many reasons why some mass-radius pairs might not be physical. For example, a neutron star's radius has to be larger than its own Schwarzschild radius, else it would be a black hole. In practice, only the two tightest constraints are important. The first one is *causality*, which is the requirement that the speed of sound must be less than c . Because c_s is defined as $\sqrt{\partial P/\partial \rho}$, while $P(\rho)$ depends on the *unknown* EoS, this requirement is somewhat arbitrary. I will use the expression given by Heinke et al. (2006): $R < 3.04 GM/c^2$. The other important constraint is set by the fastest-rotating neutron star known, the 716 Hz pulsar J1748-2446 ad. Lattimer and Prakash (2007) found that neutron stars have a minimum spin period (and hence a *maximum* spin frequency), which depends on their mass and radius. Turning this relationship around, they were able to limit NS masses and radii. Figure 12 shows the 99% probability contours of each model, with the unphysical regions clearly indicated. Although large parts of the confidence intervals have been excluded, the best-fit mass-radius pairs are all allowed.

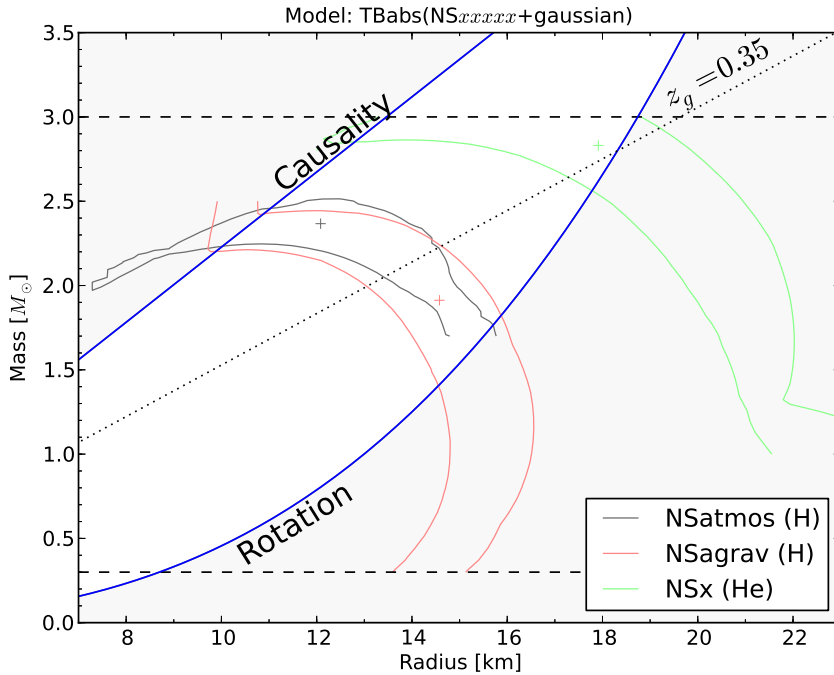


Figure 12: 99% probability contours for each model. The upper-left region, $R < 3.04 GM/c^2$, is excluded by the requirement of causality. The lower-right region shows the region $R > R_{max}$ excluded by the fastest-rotating neutron star known. The dotted line shows mass-radius pairs with $z_g = 0.35$, as determined by gravitationally redshifted absorption lines during X-ray bursts (Cottam et al., 2002). The dashed lines show the minimum (for *nsagrav*) and maximum (for *nsatmos* and *nsx*) radius for which NS atmosphere models are calculated.

The final step is to overplot a range of theoretical EoSs. I have used nine dense matter equations of state, which are summarised in Table 9. I have used a wide variety of chemical compositions, including a self-bound ‘quark star’ model (SQM3). Figure 13 shows the result.

Table 9. Dense matter equations of state (taken from Lattimer and Prakash, 2001)

Symbol	Reference	Approach	Composition
AP(3-4)	Akmal & Pandharipande (1997)	Variational	np
GM3	Glendenning & Moszkowski (1991)	Field theoretical	npH
GS1	Glendenning & Schaner-Bielich (1999)	Field theoretical	npK
MPA1	Müther, Prakash & Ainsworth (1987)	Dirac-Brueckner HF	np
MS(0-1)	Müller & Serot (1996)	Field theoretical	np
PAL1	Prakash et al. (1988)	Schematic potential	np
SQM3	Prakash et al. (1995)	Quark matter	Q (u, d, s)

Notes. ‘Approach’ refers to the underlying theoretical technique. ‘Composition’ refers to strongly interacting components (n = neutron, p = proton, H = hyperon, K = kaon, Q = quark). All models include leptonic contributions.

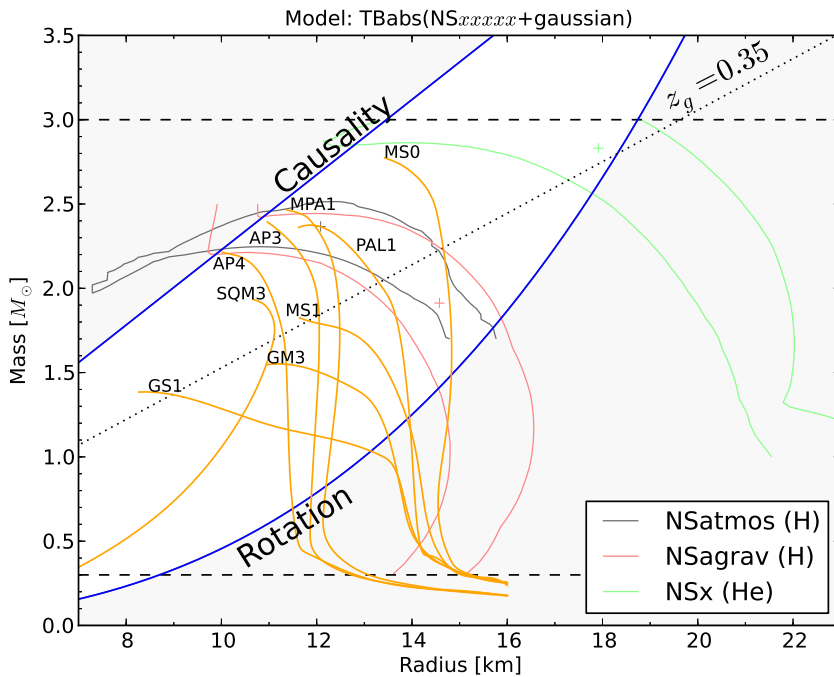


Figure 13: 99% probability contours for each model. See the caption of Figure 12 for definitions. The solid orange lines represent predictions for the masses and radii of neutron stars using the equations of state described in Table 9 (Lattimer and Prakash, 2001, 2007).

Clearly, not even the most ‘stiff’ equation of state is able to account for the mass and radius predicted by the helium model. Therefore, I conclude that the NS atmosphere of EXO 0748-676 is mainly composed of hydrogen. What is more, the only EoSs that coincide with the 99% probability contours of the hydrogen atmosphere models are those that are composed of neutrons and protons. Therefore, I conclude that the NS core’s and crust’s primary components are nucleons.

5.3 Origin of the emission line

A question that is still unanswered, is where the gaussian line shape originates from. It could well be an actual emission line, but Díaz Trigo et al. (2011) stated that the odds of detecting narrow line features from the NS surface are low, given EXO 0748-676's high spin and inclination. None of the relevant parameters (see Tables 6-8) are zero within their 90% confidence intervals, so I know there is *something*. In order to draw my own conclusion, I will analyse all possibilities.

POSSIBLE CAUSES

- Not real: the gaussian line shape might be an instrumental artefact. The maximum error in the *relative effective area* is $\pm 3\%$ ($\pm 2\%$) for the MOS (pn) cameras, as stated by the official documentation on the EPIC calibration status.⁵ Since all best-fit models found a gaussian contribution to the total flux of 6% or more for at least one of the observations, the chances of the line coming from a calibration uncertainty are slim.
- Not real: imperfections in the abundance and cross-section tables might cause a gaussian line shape. To illustrate this, I have included an image of the Crab Nebula X-ray flux spectrum, along with a model that incorporates interstellar absorption by several elements, see Figure 14.⁶ Clearly, different elements (or isotopes, for that matter) absorb at different energies. Most elements show a clear *absorption edge*: a sharp discontinuity in the absorption spectrum. They occur at wavelengths where the energy of an absorbed photon corresponds to an electronic transition. A slightly more energetic photon still has a small chance to be absorbed, hence the tail of, for example, Ne's absorption feature. It is easy to see that, if some of the abundances and/or cross-sections were slightly off, one or more of these features might be a little stronger (i.e. 'deeper') than they should be. In that case, XSPEC compensates by detecting an emission feature at the same energy.

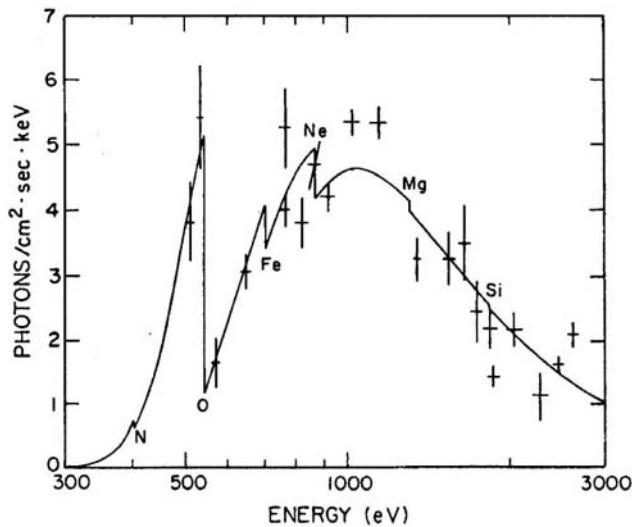


Figure 14: The X-ray flux spectrum of the Crab Nebula (crosshairs), along with an interstellar absorption model (solid line)

This explanation is plausible, as all models contain an interstellar absorption component (*tbabs*), and a gaussian line was detected in each of the models. It also explains *why* the residuals were approximately gaussian. Furthermore, assuming that the solar abundance vector is a good approximation of the ISM abundance vector is bound to introduce errors.

⁵Taken from <http://xmm2.esac.esa.int/docs/documents/CAL-TN-0018.pdf>

⁶Picture taken from the SPIE digital library

- Not real: the gaussian line shape might stem from a flaw in the NS atmosphere components. Despite modellers' best efforts, NS atmosphere calculations are still simplistic. They treat a three-dimensional problem as one-dimensional and make many assumptions. Moreover, they are not done 'on the spot', but interpolated from discrete data sets. All this makes the NS atmosphere component prone to errors. This explanation, however, does not directly explain the shapes of the residuals.
- Real: the gaussian line profile is caused by an emission line from the NS surface. Real spectral lines are broadened because energy levels are not infinitely sharp (due to quantum mechanical uncertainties) and because atoms move relative to the observer (Doppler effect). The latter relates the width of a spectral line to the velocity dispersion of a collection of objects. Hence,

$$\frac{\sigma}{E} \approx \frac{v}{c},$$

where σ and E are the line width and energy, respectively, of the spectral feature, and v the speed of the emitting (or absorbing) material. In this case, I should consider the speed of the NS surface, so that,

$$\frac{\sigma}{E} \approx \frac{v_{rot,eq}}{c} = \frac{2\pi\nu_{spin} \times R_{NS}}{c},$$

where $v_{rot,eq}$ is the rotational velocity at the neutron star's equator and ν_{spin} is its spin frequency, which Galloway et al. (2010) reported to be 552 Hz. If the gaussian line originated from the NS surface, both sides of the equation *should* be approximately equal:

- *nsatmos*: $0.50 \approx 0.14$
- *nsagrav*: $0.63 \approx 0.17$
- *nsx*: $0.26 \approx 0.21$

Unfortunately, it turns out that Doppler broadening can only explain the line of the helium atmosphere model, which I have already discarded. The other two lines are 'too broad'. This makes it implausible that they originate from the NS surface. It is, however, not ruled out, as there might be other processes at play. A spectral line can also be broadened by collisional broadening, and even by general relativistic effects such as light-bending, see e.g. Bhattacharyya et al. (2005). Which element, then, might be responsible for such a line? I will first use the model's best-fit masses and radii to compute gravitational redshifts, and then use these to convert the observed line energies (E_{obs}) to the energies at which they were emitted (E_{rest}). I will then compare these values to tables of strong X-ray spectral lines. Because of the extremely high temperature of the NS surface, I will only consider the highly ionised H- and He-like species. The formula for gravitational redshift is:

$$z_g = \frac{1}{\sqrt{1 - \frac{2GM}{c^2 R}}} - 1$$

This yields gravitational redshifts of 0.54, 0.28 and 0.37, respectively, for the three models. Using $E_{rest} = E_{obs}/(1 + z_g)$, the unredshifted line energies become 0.23, 0.25 and 0.34 keV. Comparing this to the tables, I conclude that they were most likely produced by either carbon V or carbon VI. Because I have not taken any uncertainties into consideration, this result might not be reliable. Note that I assume the *cosmological* redshift to be zero, which is a good approximation for a distance of only 7.1 kpc.

- Real: same as the above, but from somewhere else in the environment of the neutron star, e.g. from a weak residual accretion disc. I will use the same method for the most part, but in this case, I should consider the *orbital* velocity of the emitting material,

$$\frac{\sigma}{E} \approx \frac{v_{orb}}{c},$$

where v_{orb} is given by Kepler's law:

$$\Omega_{orb} = \sqrt{\frac{GM}{d^3}} \implies v_{orb} = d\Omega_{orb} = \sqrt{\frac{GM}{d}}$$

$$\frac{\sigma}{E} \approx \frac{1}{c} \sqrt{\frac{GM}{d}},$$

where Ω_{orb} is the angular orbital velocity of the material and d is the distance from the centre of mass of the LMXB to the rotating matter. Since this expression depends on d , I cannot simply calculate its right-hand side. Instead, I will just assume that the lines have been 'properly' broadened, and focus on their possible origin. I will take the gravitational redshift in the limit that the circling material is infinitely far away,

$$\lim_{d \rightarrow \infty} z_g = \lim_{d \rightarrow \infty} \frac{1}{\sqrt{1 - \frac{2GM}{c^2 d}}} - 1 = 0$$

In that case, the lines were emitted at the same energy as they were observed, namely at 0.36, 0.32 and 0.47 keV, respectively. Comparing this to the tables, I conclude that they were most likely produced by either ionised carbon or ionised nitrogen atoms. Had I taken a different redshift, this result would not have changed. Again, no uncertainties were considered, so this result might be unreliable.

Taking everything together, I conclude that the gaussian line profile most likely stems from imperfections in the abundance and cross-section tables. If they are, on the other hand, real, they must have been produced by the lightest X-ray emitting atoms, those being highly ionised carbon and nitrogen. The unlikeliness of any residual accretion favors the former.

6 CONCLUSIONS

I have analysed four observations of EXO 0748-676 spanning over four years, after it started transitioning from outburst to quiescence. I conclude that:

- The observed X-ray spectra can indeed be reproduced with cooling NS models, modified by interstellar absorption.
- A NS helium atmosphere model provides fits as good as hydrogen atmosphere models, but predicts a heavier and larger neutron star.
- The most recent accretion phase cannot by itself account for the mass reached by the neutron star.
- None of the proposed EoSs for dense, cold nuclear matter can account for the the mass and radius predicted by the helium atmosphere model.
- The internal composition of the neutron star appears to be dominated by neutrons and protons, rather than by hyperons, kaons or quark matter.
- The most likely explanation for the gaussian line component, which was found to improve all fits, is that it stems from imperfections in the abundance and cross-section tables used to describe the ISM. If it is a real emission line, it is produced by ionised carbon or nitrogen.

APPENDICES

A Spectral fitting and XSPEC

When measuring the spectrum of a source, a spectrometer does not measure the actual spectrum, $f(E)$. The actual spectrum is distorted by the instrument response, $R(I, E)$, which is proportional to the probability that an incoming photon of energy E will be detected in instrument channel I . What the spectrometer does obtain, is photon counts within specific instrument channels, $C(I)$. The observed spectrum is related to the actual spectrum by:

$$C(I) = \int_0^{\infty} f(E)R(I, E)dE$$

The goal of spectral fitting is to determine the actual spectrum of the source ($f(E)$) for a given observed spectrum ($C(I)$). Since, in general, inverting this equation is not possible, one has to find an alternative way to work out $f(E)$. The usual alternative is to choose a parametrised *model* spectrum $M(E; p_1, p_2, \dots)$ and match, or ‘fit’ it to the observed spectrum by varying the values of the parameters. Some ‘fit statistic’ is used to measure how well they compare. The most common way to determine the ‘best-fit’ model is by minimising (locally) χ^2 , defined as:

$$\chi^2 = \sum \frac{(C(I) - C_p(I))^2}{\sigma(I)^2},$$

where $C_p(I)$ is the predicted count spectrum, calculated for each $M(E)$ (in units of photons $\text{cm}^{-2} \text{s}^{-1}$), and $\sigma(I)$ is the error for channel I , usually estimated by $\sqrt{C(I)}$. By using this fit statistic, one assumes that all spectral channels are Gaussian distributed and that the variance is uncorrelated with the observed counts. The confidence interval for a given parameter is computed by varying the parameter value until χ^2 increases by a particular amount above the minimum value. The critical $\Delta\chi^2$ for common cases is given in the following table (Avni, 1976):

Table 10. Critical $\Delta\chi^2$ for common cases

Confidence	Parameters		
	1	2	3
0.68	1.00	2.30	3.50
0.90	2.71	4.61	6.25
0.99	6.63	9.21	11.30

All this is implemented in the X-ray spectral fitting package XSPEC, albeit in a slightly more complicated way. Basically, XSPEC needs four files in order to work. Two of these are used to obtain the observed spectrum, $C(I)$, and the other two to construct the detector response, $R(I, E)$. A different program must be used to create these files. To obtain the observed spectrum, one needs the **data (spectrum) file**, containing $D(I)$, and the **background file**, containing $B(I)$. The background-subtracted count rate is then given by:

$$C(I) = \frac{D(I)}{a_{D(I)}t_D} - \frac{b_{D(I)}}{b_{B(I)}} \frac{B(I)}{a_{B(I)}t_B},$$

where $D(I)$ and $B(I)$ are the counts in the data and background files, t_D and t_B are the respective exposure times, and the a ’s and b ’s are the **area** and **background scaling** values which refer the background flux to the same area as the observation.

To predict the spectrum that would be detected by a given instrument ($C_p(I)$), given a model spectrum ($M(E)$), XSPEC must know the specific characteristics of the instrument. This information is contained in two files: the **response file** and the **auxiliary response file**.

The response ($R(I, E)$) is a continuous function of E . It is converted to a discrete function by the creation of a response *matrix*,

$$R_D(I, J) = \frac{\int_{E_{J-1}}^{E_J} R(I, E) dE}{E_J - E_{J-1}}$$

The response file contains the energy ranges, E_J , and the response matrix, $R_D(I, J)$. The auxiliary response file contains an array, $A_D(J)$, designed to represent the efficiency of the detector, that is multiplied into $R_D(I, J)$ as follows:

$$R_D(I, J) \rightarrow R_D(I, J) \circ A_D(J)$$

Once data have been read in and a model defined, the *fit* command is used to start the fitting algorithm. At the end of a fit, XSPEC writes out the best-fit parameter values. The *error* command can then be used to estimate confidence intervals. To compute confidence regions for several (possibly correlated) parameters at the same time, one can use the *steppar* command.

B Uncertainty calculations

The XSPEC command *error* is used to determine the confidence region for a model parameter. However, if one aims to compute the uncertainty in a *derived* quantity, one has to resort to other measures. In my case, these derived quantities are kT_{eff}^∞ and the fluxes. kT_{eff}^∞ does not only depend on the model parameter T_{eff} , but also (through gravitational redshift) on the mass and radius of the neutron star. The fluxes are not calculated by fitting a model parameter, but by issuing the *flux* command. Admittedly, XSPEC contains the *cflux* component, which should solve this issue. Defining the model as e.g. *tbabs * cflux * (nsatmos + gaussian)* or *tbabs * (nsatmos + cflux * gaussian)* would yield F_{tot} or F_{gauss} , respectively. The errors can then be calculated in the usual way. However, using the *cflux* component drastically changes all best-fit parameters, which might make the results unreliable. Therefore, I resort to an approximate method, known as the *variance formula*, for both kT_{eff}^∞ and the fluxes. It assumes that the variables are uncorrelated and that the errors are Gaussian (which is not true). Hence,

$$f = f(T_{eff}, M, R)$$

$$\sigma_f^2 = \left(\frac{\partial f}{\partial T_{eff}} \right)^2 \sigma_{T_{eff}}^2 + \left(\frac{\partial f}{\partial M} \right)^2 \sigma_M^2 + \left(\frac{\partial f}{\partial R} \right)^2 \sigma_R^2$$

We have that, for example,

$$\frac{\partial f}{\partial M} \cong \frac{f(T_{eff}, M \pm \Delta M, R) - f(T_{eff}, M, R)}{\Delta M}$$

Now take $\Delta M = \sigma_M$,

$$\frac{\partial f}{\partial M} \approx \frac{f(T_{eff}^0, M^0 \pm \sigma_M, R^0) - f(T_{eff}^0, M^0, R^0)}{\sigma_M},$$

where the 0's denote the best-fit values. So,

$$\begin{aligned} \sigma_f^2 &= \left(\frac{f_T - f_0}{\sigma_{T_{eff}}} \right)^2 \cancel{\sigma_{T_{eff}}^2} + \left(\frac{f_M - f_0}{\sigma_M} \right)^2 \cancel{\sigma_M^2} + \left(\frac{f_R - f_0}{\sigma_R} \right)^2 \cancel{\sigma_R^2} \\ &= (f_T - f_0)^2 + (f_M - f_0)^2 + (f_R - f_0)^2, \end{aligned}$$

where f_0 is short for $f(T_{eff}^0, M^0, R^0)$, f_T for $f(T_{eff}^0 \pm \sigma_{T_{eff}}, M^0, R^0)$, et cetera. For kT_{eff}^∞ , these values can be calculated analytically. For the fluxes, I have to modify the parameter values in XSPEC and then run the *flux* command. To obtain unabsorbed fluxes, N_H must be set to zero.

REFERENCES

- Anders, E. and Grevesse, N. (1989). Abundances of the elements - Meteoritic and solar. *Geochimica et Cosmochimica Acta*, 53:197–214.
- Arnaud, K. A. (1996). XSPEC: The First Ten Years. In *Astronomical Data Analysis Software and Systems V*, volume 101 of *Astronomical Society of the Pacific Conference Series*, pages 17–20.
- Avni, Y. (1976). Energy spectra of X-ray clusters of galaxies. *The Astrophysical Journal*, 210:642–646.
- Balucinska-Church, M. and McCammon, D. (1992). Photoelectric absorption cross sections with variable abundances. *The Astrophysical Journal*, 400:699–700.
- Bhattacharyya, S., Miller, M. C., and Lamb, F. K. (2005). Surface Atomic Spectral Lines from Weakly Magnetic Rotating Neutron Stars. In *X-ray Diagnostics of Astrophysical Plasmas: Theory, Experiment, and Observation*, volume 774 of *American Institute of Physics Conference Series*, pages 291–293.
- Brown, E. F. and Cumming, A. (2009). Mapping Crustal Heating with the Cooling Light Curves of Quasi-Persistent Transients. *The Astrophysical Journal*, 698:1020–1032.
- Cottam, J., Paerels, F., and Mendez, M. (2002). Gravitationally redshifted absorption lines in the X-ray burst spectra of a neutron star. *Nature*, 420:51–54.
- Díaz Trigo, M., Boirin, L., Costantini, E., Méndez, M., and Parmar, A. (2011). XMM-Newton observations of the low-mass X-ray binary EXO 0748-676 in quiescence. *Astronomy and Astrophysics*, 528:A150.
- Díaz Trigo, M., Parmar, A. N., Boirin, L., Méndez, M., and Kaastra, J. S. (2006). Spectral changes during dipping in low-mass X-ray binaries due to highly-ionized absorbers. *Astronomy and Astrophysics*, 445:179–195.
- Galloway, D. K., Lin, J., Chakrabarty, D., and Hartman, J. M. (2010). Discovery of a 552 Hz Burst Oscillation in the Low-Mass X-Ray Binary EXO 0748-676. *The Astrophysical Journal Letters*, 711:L148–L151.
- Galloway, D. K., Muno, M. P., Hartman, J. M., Psaltis, D., and Chakrabarty, D. (2008a). Thermonuclear (Type I) X-Ray Bursts Observed by the Rossi X-Ray Timing Explorer. *The Astrophysical Journal Supplement Series*, 179:360–422.
- Galloway, D. K., Özel, F., and Psaltis, D. (2008b). Biases for neutron star mass, radius and distance measurements from Eddington-limited X-ray bursts. *Monthly Notices of the Royal Astronomical Society*, 387:268–272.
- Güver, T. and Özel, F. (2009). The relation between optical extinction and hydrogen column density in the Galaxy. *Monthly Notices of the Royal Astronomical Society*, 400:2050–2053.
- Heinke, C. O., Rybicki, G. B., Narayan, R., and Grindlay, J. E. (2006). A Hydrogen Atmosphere Spectral Model Applied to the Neutron Star X7 in the Globular Cluster 47 Tucanae. *The Astrophysical Journal*, 644:1090–1103.
- Ho, W. C. G. and Heinke, C. O. (2009). A neutron star with a carbon atmosphere in the Cassiopeia A supernova remnant. *Nature*, 462:71–73.
- Lattimer, J. M. and Prakash, M. (2001). Neutron Star Structure and the Equation of State. *The Astrophysical Journal*, 550:426–442.
- Lattimer, J. M. and Prakash, M. (2007). Neutron star observations: Prognosis for equation of state constraints. *Physics Reports*, 442:109–165.

- Parmar, A. N., White, N. E., Giommi, P., and Gottwald, M. (1986). The discovery of 3.8 hour periodic intensity dips and eclipses from the transient low-mass X-ray binary EXO 0748-676. *The Astrophysical Journal*, 308:199–212.
- Strüder, L., Briel, U., Dennerl, K., Hartmann, R., Kendziorra, E., Meidinger, N., Pfeffermann, E., Reppin, C., Aschenbach, B., Bornemann, W., Bräuning, H., Burkert, W., Elender, M., Freyberg, M., Haberl, F., Hartner, G., Heuschmann, F., Hippmann, H., Kastelic, E., Kemmer, S., Kettenring, G., Kink, W., Krause, N., Müller, S., Oppitz, A., Pietsch, W., Popp, M., Predehl, P., Read, A., Stephan, K. H., Stötter, D., Trümper, J., Holl, P., Kemmer, J., Soltau, H., Stötter, R., Weber, U., Weichert, U., von Zanthier, C., Carathanassis, D., Lutz, G., Richter, R. H., Solc, P., Böttcher, H., Kuster, M., Staubert, R., Abbey, A., Holland, A., Turner, M., Balasini, M., Bignami, G. F., La Palombara, N., Villa, G., Buttler, W., Gianini, F., Lainé, R., Lumb, D., and Dhez, P. (2001). The European Photon Imaging Camera on XMM-Newton: The pn-CCD camera. *Astronomy and Astrophysics*, 365:L18–L26.
- Titarchuk, L. (1994). Generalized Comptonization models and application to the recent high-energy observations. *The Astrophysical Journal*, 434:570–586.
- Turner, M. J. L., Abbey, A., Arnaud, M., Balasini, M., Barbera, M., Belsole, E., Bennie, P. J., Bernard, J. P., Bignami, G. F., Boer, M., Briel, U., Butler, I., Cara, C., Chabaud, C., Cole, R., Collura, A., Conte, M., Cros, A., Denby, M., Dhez, P., Di Coco, G., Dowson, J., Ferrando, P., Ghizzardi, S., Gianotti, F., Goodall, C. V., Gretton, L., Griffiths, R. G., Hainaut, O., Hochedez, J. F., Holland, A. D., Jourdain, E., Kendziorra, E., Lagostina, A., Laine, R., La Palombara, N., Lortholary, M., Lumb, D., Marty, P., Molendi, S., Pigot, C., Poindron, E., Pounds, K. A., Reeves, J. N., Reppin, C., Rothenflug, R., Salvatat, P., Sauvageot, J. L., Schmitt, D., Sembay, S., Short, A. D. T., Spragg, J., Stephen, J., Strüder, L., Tiengo, A., Trifoglio, M., Trümper, J., Vercellone, S., Vigroux, L., Villa, G., Ward, M. J., Whitehead, S., and Zonca, E. (2001). The European Photon Imaging Camera on XMM-Newton: The MOS cameras : The MOS cameras. *Astronomy and Astrophysics*, 365:L27–L35.
- Verner, D. A., Ferland, G. J., Korista, K. T., and Yakovlev, D. G. (1996). Atomic Data for Astrophysics. II. New Analytic FITS for Photoionization Cross Sections of Atoms and Ions. *The Astrophysical Journal*, 465:487–498.
- Wilms, J., Allen, A., and McCray, R. (2000). On the Absorption of X-Rays in the Interstellar Medium. *The Astrophysical Journal*, 542:914–924.
- Yan, M., Sadeghpour, H. R., and Dalgarno, A. (1998). Photoionization Cross Sections of He and H₂. *The Astrophysical Journal*, 496:1044–1050.
- Zavlin, V. E., Pavlov, G. G., and Shibano, Y. A. (1996). Model neutron star atmospheres with low magnetic fields. I. Atmospheres in radiative equilibrium. *Astronomy and Astrophysics*, 315:141–152.